ORIGINAL PAPER

Shaking table test study of accumulation layer landslide under earthquake action

Kun Ma[1] · Yongmou Zhang[1] · Honggang Wu[2] · Zhiyang Ji[1] · Jiankai Ren[1] · Yu Liang[1] · Xinlu Zhou[1]

Abstract
China is located at the intersection of the Pacific Rim and Eurasian seismic belts. The compression and tension between plates have caused the development of fault zones. High frequency, wide distribution, and strong activity have become the main characteristics of China's seismic activity. A landslide in Yushu area of Qinghai Province, China, is selected as the main research object and engineering example. This research takes softening effect of dynamic load on the strength of rock, soil, and the law of seismic wave propagation in slope as theoretical basis. The actual damage characteristics of slope in the earthquake are the basis as well. The geomechanics theory is used to simplify the geomechanics model, and large-scale shaking table test is used to carry out the study of instability mechanism. Combined with the FLAC3D elastoplastic theory, the following conclusions are mainly drawn: (1) single slip surface under earthquake, the deformation characteristics of accumulation layer landslide are cracks in the middle of slope→development toward the front edge of slope→deformation of the trailing edge of traction→tension cracks; (2) according to calculation of the point safety factor, the sliding process of the 2# landslide, it exhibits the characteristics of pushing slip, and the sliding mechanism of accumulation landslide is not affected during earthquake; and (3) the slip zone soil has an obvious blocking effect on acceleration amplification effect of the landslide body.

Keywords Earthquake action · Single slip surface · Accumulation layer landslide · Shaking table test · FLAC3D · Point safety factor method

Introduction

China is located at the intersection of the Pacific Rim and the Eurasian seismic belt (Huang et al. 2008). Since the twentieth century, nearly 800 earthquakes of magnitude 6 or above have occurred in China (Wang 2012; Ma and Ma 2007; Sui 2009; Xiong 2009). At present, the academic research on the dynamic response of slopes under the influence of earthquakes mainly focuses on theoretical

✉ Honggang Wu
271462550@qq.com

1 School of Civil Engineering, Lanzhou Jiaotong University, Gansu 730000, People's Republic of China

2 Northwest Railway Academy Co., Ltd of CREC, 730000 Gansu, People's Republic of China

research and model tests (Li 1999; Liu et al. 2007). For example: Celebi 1987. Based on typical engineering cases, through data testing and theoretical calculation and analysis, it is concluded that seismic waves have an amplifying effect due to terrain conditions. Liu and Zhu (1999) have done a lot of research work on site effect, terrain effect, incident wave type, incident direction, angle of incidence, height of underground cover, adjacent terrain, and three-dimensional effects of terrain. In the aspect of seismic wave slope instability mechanism research, Hutchinson (1989) put forward the mechanism of instability and slip-page induced by soil liquefaction through on-site landslide test data and indoor model test verification; Hu (1995) calculated from theoretical calculations, model tests, and numerical calculations have revealed the differences in the deformation and instability mechanisms of slopes under earthquake action. Zhang et al. (1993) summarized and analyzed a large number of engineering examples and revealed the performance of slope stability caused by earthquake action. It is the cumulative effect and the

Table 1 Comparison of various stability coefficient calculation methods (Del Gaudio and Wasowski 2007; Cai et al. 2002)

Calculation method	Slip surface morphology	Strip form	Whether to consider the force between the bars	Boundary conditions
Swedish arc method	Arc	Complete	Not considered	
Swedish section method	Arc	Vertical strip	Not considered	
Bishop method	Arc	Vertical strip	Consideration	
Simple distribution method	Arc, non-circular	Vertical strip	Consideration	
Inference transfer method	Polygonal-shape	Vertical strip	Consideration	
Sarma method	Any complex form	Vertical or non-vertical	Consideration	Homogeneous boundary
Msanma method	Any complex form	Vertical or non-vertical	Consideration	Nonhomogeneous boundary

triggering effect. Mao et al. (2001) demonstrated and discussed the mechanism of ground motion-induced landslide movement. Qi et al. (2004) believe that the instability of the seismic slope is caused by the rapid accumulation of seismic inertial force and excess pore water pressure.

In view of the natural disasters of landslides, in order to evaluate the degree of landslide risk in different areas, it is necessary to analyze and evaluate the stability of the landslide, and then provide a theoretical basis for the treatment of the landslide. The methods and theories of stability analysis commonly used worldwide are shown in Table 1.

The numerical analysis method is an improvement and supplement to the limit equilibrium method. The following methods have been used more maturely: finite element method (FEM), boundary element method (BEM), and discrete element method (DEM) (Gong 2001).

1. The research and application of finite element method has an important relationship with the emergence and application of finite element calculation technology (Zheng and Zhao 2004).
2. The discrete element method was proposed by scholars such as Cundall (Coates 1970) in 1971.
3. The boundary element method has appeared as early as the 1970s, and it is essentially a branch of the weighted residual method.

The limit analysis method mainly includes the following three parts: first, the slip line method (Chen 2003; Sokolovsky 1956); second, through the study and analysis of slope stability, explore the upper limit of plastic mechanics; and third, through the development of limited Meta-analysis, established the upper and lower limit analysis method (Sloan 1989a; Sloan 1989b).

For the study of slope rock mass structure theory, domestic scholars (Sun 1988; Sun and Gu 1980) applied in-depth theoretical knowledge to the protection of slope engineering. Shi (1977) proposed a slope or a new method of chamber reinforcement; in addition, Luo et al. (1981) and Li (1997) put forward a deterministic theory closer to the actual state

of the project through the study of the relevant theoretical system of slopes.

In addition to the above research theories and methods, many theories and methods such as field monitoring method and artificial neural network method are also widely used in engineering (H and C et al. 2004).

Xia et al. (1995), Xun and Mou et al. (1988), and Sun (2007) conducted in-depth research on the relevant theories of earthquake engineering through theoretical analysis and shaking table tests. Clough and Pirtz (1956) studied the seismic effects of different dams on the basis of physical model tests. Seed and Clough (1963) conducted an in-depth study on the seismic effect of the core dam through shaking table tests. Subsequently, Arango and Seed (1974) used shaking table tests to obtain the mechanical image of the slope in the deformed state. Wartman et al. (2005) conducted a shaking table physical model test to study the principle and applicability of earthquake-induced slope deformation. Wang and Lin (2011) and Lin and Wang (2006) used the shaking table slope test and used the acceleration time history curve to study the slope balance theory. Many Chinese experts and scholars have also carried out a lot of research work on this: Xu et al. (2008) and Zhang and Wu (1997) used large-scale shaking table tests to study the dynamic response of landslides under earthquake action. Feng et al. (2009) and Chen et al. (2010) also used shaking table tests to conduct an in-depth study on the slope response mechanism under earthquake action.

In recent years, with the continuous improvement of test conditions, many scholars have extensively carried out shaking table test research. Keefer (1984) and Shimizu et al (1986) carried out shaking table tests to refine the criteria for the dynamic stability of slopes. After the Wenchuan earthquake in 2008, China paid more attention to shaking table tests: Dong et al. (2011), Yang et al. (2012a), and Yang et al. (2012b) used the shaking table test to determine the dynamic response of homogeneous, bedding, and anti-dip slopes. After in-depth analysis, Yang et al. (2013a), (2013b), (2013c), and Ye et al. (2012a, b, c) took different types of rock slopes as basic research objects, and made an in-depth
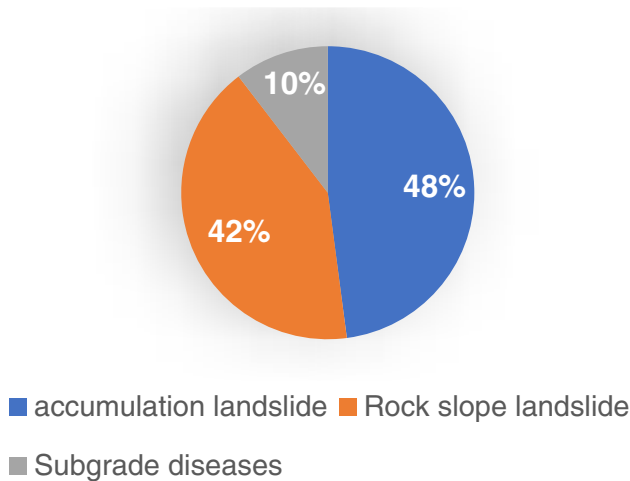
Fig. 1 Statistical map of geological disasters along the highway after the earthquake

analysis of the slope instability mechanism by means of shaking table tests. The study combined with the discrete element calculation; the instability mechanism of the rock slope caused by the earthquake is summarized. In addition, Hong et al. (2005), Ling et al. (2005), Ye et al. (2011), Ye et al. (2012a, b), Qu and Zhang (2012), and Qu et al. (2013) used large-scale shaking table tests to study the influence of foundation conditions on the seismic earth pressure of retaining walls.

Urgently, this article takes the deformed slope of a landslide in Yushu area, Qinghai Province, China as the main research object and engineering example. The softening effect of dynamic load on the strength of rock and soil and the propagation law of seismic waves in the slope are taken as The theoretical basis is based on the actual failure

characteristics of the slope in an earthquake. The geomechanical theory is used to simplify the geomechanical model, combined with the FLAC3D elastoplastic theory, and the mechanism of slope instability under seismic action has been studied through large-scale shaking table tests.

Overview of landslide sites and basic characteristics of the Yushu earthquake

Overview of landslides in Qinghai Yushu Airport

In the early morning of April 14, 2010, an earthquake with a magnitude of 7.1 occurred in Yushu, Qinghai. The earthquake slope disaster caused multiple traffic interruptions, which seriously affected the development of earthquake disaster relief work. According to statistics, a total of 48 side (landslide) sites were investigated and analyzed along the highway after the Yushu earthquake, including 23 landslides in the accumulation layer of the canyon section; 20 diseases such as rock mass dumping, dangerous rock mass, and broken rock landslides; plateau freezing There are 5 problems of roadbed (embankment) deformation and cracking in soil area (Fig. 1).

Therefore, this model experiment is based on the No. 2 landslide in Qinghai Yushu Airport Section as the prototype. The landslide belongs to the accumulation layer landslide caused by the earthquake. The landslide body is almost perpendicular to the road surface. The width of the parallel route is about 482 m, the longitudinal length is about 85 m, the thickness of the sliding body is about 18 m, and the volume of the sliding body is about 54.2×104 m³. The entire landslide is divided into front and back stages by the
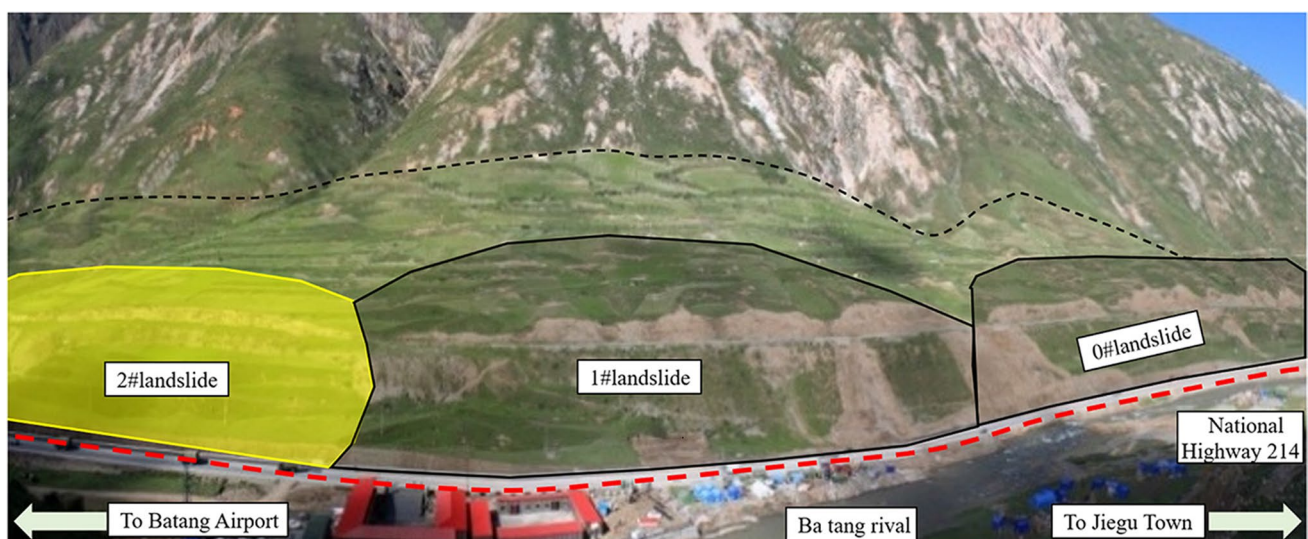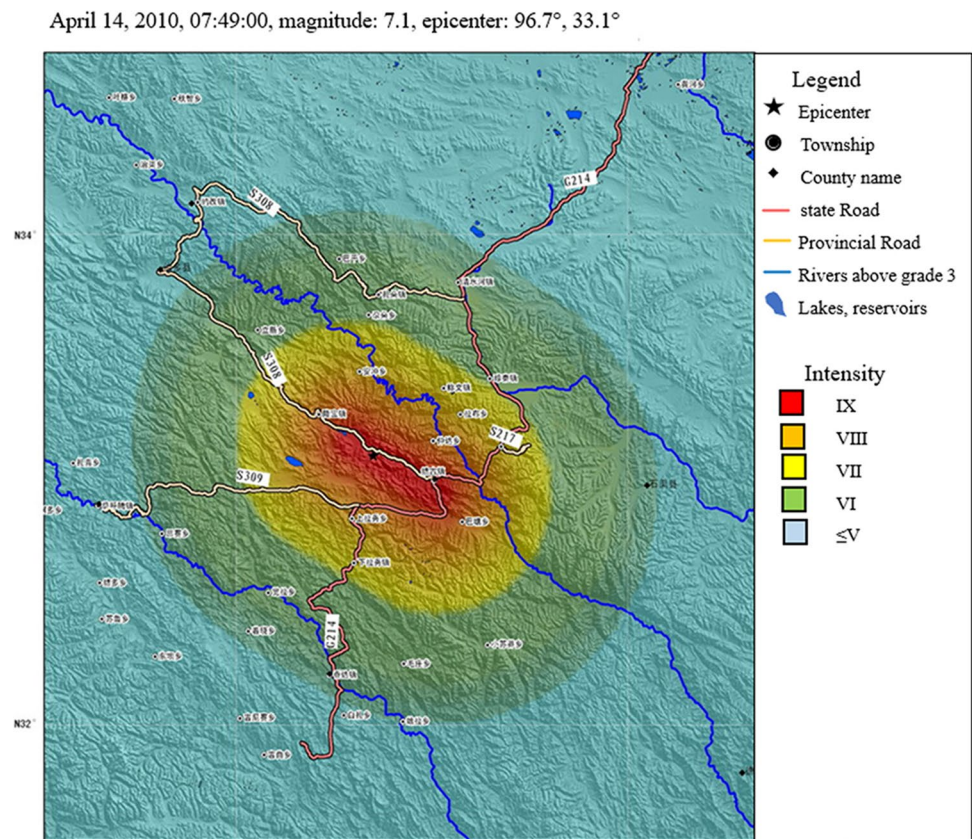

Fig. 2 A complete view of No.2 accumulation landslide

Fig. 3 Distribution diagram of coseismatic displacement intensity (Zhang et al. 2010)

April 14, 2010, 07:49:00, magnitude: 7.1, epicenter: 96.7°, 33.1°

diversion canal of Xihang Power Station. The front stage is mainly distributed on the outside of the diversion canal of Xihang Power Station, and the back stage is distributed on the inner side of the diversion canal of Xihang Power Station. Figure 2 shows the overall view of the No. 2 landslide in the Yushu Airport section of Qinghai.

Basic characteristics of the Yushu M7.1 earthquake

Seismological and geological background

Yushu County is located in the Qinghai-Tibet Sichuan-Yunnan-Batang depression fold belt. Judging from the projection of the slippage (dislocation) on the fault plane on the surface, the two rupture areas are located near the epicenter and 10–30 km southeast of the epicenter, respectively. The rupture of the earthquake mainly spread to the southeast. It shows that the rupture of this earthquake mainly expanded to the southeast, causing large losses and casualties.

Focal mechanism, rupture process and seismic intensity

According to the data, the scalar seismic moment of the earthquake is about 4.4×1019 Nm and the moment magnitude is 7.0. The two nodal planes that characterize the focal mechanism are strike 119°/dip angle 83°/

slip angle − 2° and strike 209°/inclination angle 88°/slip angle − 173° (Zhang et al. 2010). After the Yushu M7.1 earthquake in Qinghai, the China Seismic Network Center quickly released the coseismic intensity distribution map of this earthquake, as shown in Fig. 3, which takes into account the local site effect, focal mechanism and focal rupture process. According to Ma et al. (2018, 2019), the ground motion induced at a certain location is controlled by the dual effects of azimuth, source distance and source magnitude.

Experimental designs of shaking table

Overview of shaking table

This shaking table model test uses the large-scale earthquake simulation shaking table of the Lanzhou Seismological Research Institute of Gansu Seismological Bureau. The size of the vibrating table is 4 m × 6 m, the maximum bearing capacity is 25 t, the maximum acceleration is 1.7 g, the maximum speed is 1.5 m/s, and the maximum displacement is 250 mm in the X direction and 100 mm in the Z direction. Regular and irregular waves can be input. The effective frequency range is 0.1 ~ 50 Hz. The main control indicators of the shaker are shown in Table 2 below.

Experimental model design

Experimental similarity ratio

Combining the technical parameters of the shaking table in the laboratory and the slope prototype, the geometric similarity ratio is selected as:

$$C_L = \frac{L_P}{L_M} = 100$$

In the formula: C_L—geometric similarity constant;

L_P—Prototype size
L_M—model size

According to the determined geometrical similarity constant CL = 100, the similarity relationship of other physical quantities is derived from the basic dimension according to the π theorem, and the similarity parameters of the determined model design are shown in Table 3.

Design and production of experimental model

Experimental model materials are determined through multiple sets of experiments to determine similar materials such as those shown in Table 4.

The model box adopts a rigid sealed model groove with an inner groove size of 3.0 m × 1.5 m × 1.14 m. In order to facilitate observation, its long side is made of 2-cm-thick transparent glass fiber-reinforced plastic, and its surface is

Table 3 Similarity ratio of main parameters of model experiment

Physical quantity	Similarity relation	Similarity constant
Length	C_L	100
Bulk density	C_γ	1
Compression modulus	$C_E = C_L C_\gamma$	100
Acceleration	$C_a = C_E/(C_L C_\gamma)$	1
Displacement	C_S	100
Internal friction angle	C_φ	1
Cohesion	$C_E = C_L C_\gamma$	100

Table 2 Technical parameters of the vibration table test system

Indicator category	Sub-indices	Specification
Vibrating table top	Table size	6 m × 4 m
	Countertop quality	About 20 t
	Countertop material	Aluminum alloy
Acceleration transducer	Sensor form	Compression deformation acceleration sensor
	Maximum no-load acceleration	Horizontal: 4 g; Vertical: 3 g
	Measuring direction	Horizontal X direction, vertical Z direction
Horizontal vibration function	Vibration actuator	Multi-axis parallel type (AC servo motor + ball screw)
	Maximum vibration force	600 k N
	Maximum amplitude	± 250 mm
	Maximum load	25 t
	Maximum acceleration (bearing 20t)	1.7 g
	Maximum speed	1.5 m/s
	Vibration frequency (full load 25 t)	0.1 ~ 70 Hz
Vertical vibration function	Vibration actuator	Multi-axis parallel type (AC servo motor + ball screw)
	Maximum vibration force	600 k N
	Maximum amplitude	± 100 mm
	Maximum load	15 t
	Maximum acceleration (full load 15 t)	1.2 g
	Maximum speed	0.7 m/s
	Vibration frequency (full load 15 t)	0.1 ~ 50 Hz
Horizontal and vertical coupling and linkage vibration function	Vibration actuator	Multi-axis parallel type (AC servo motor + ball screw)
	Maximum amplitude	Horizontal: ± 150 mm; vertical: ± 100 mm
	Maximum acceleration (carrying 15 t)	Horizontal: 1.2 g; vertical: 1.0 g
	Maximum speed	Horizontal: 1.0 m/s; vertical: 0.7 m/s
	Vibration frequency (bearing 15 t)	Horizontal: 0.1 ~ 50 Hz; vertical: 0.1 ~ 50 Hz

Table 4 Ratio of similar materials

	Material selection	Material selection
Sliding bed	Sand: Gypsum: Talc: Glycerin: Water	80:2:5:10:3 (volume ratio)
Sliding mass	Sand: Talc: Bentonite: Water	70:26.5:0.5:3 (mass ratio)
Bedrock	Sand: Cement: Soil: Water	40:25:60:10 (mass ratio)

lined with a layer of polyethylene plastic to reduce the size of the model and the box. Contact friction between bodies. The model box and the completed model are shown in Fig. 4.

Sensor layout and working condition setting

The sensors used in this experiment mainly include acceleration sensors and earth pressure sensors. The landslide body can be divided into three parts: sliding mass, sliding bed, and bedrock. Therefore, the layout of the sensor needs to be able to capture these three parts during the vibration process. Acceleration and earth pressure response of each part, the specific location of each sensor is arranged every 40 cm from the foot of the slope to the top of the slope of the model, a total of 7 sections are arranged, and the corresponding acceleration and earth pressure sensors are arranged along each section, The specific layout position of the sensor is shown in Fig. 5 below. It should be noted that in the figure, the earth pressure sensor is identified by the letter T, and the acceleration sensor is identified by the letter J. Acceleration sensors in X and Z acquisition directions are arranged at each accelerometer measuring point. The loading conditions of seismic waves are shown in Table 5.

Analysis of test phenomena

Figure 6a shows the front view of crack development and deformation. When working condition 3 is input with 0.1 g sine wave sweep in the X direction, as the loading progresses, under the action of low-intensity earthquakes, the measurement of the sliding body in the diversion canal begins to slightly vertical cracks. When working condition 4 input 0.1 g Yushu wave sweep in X direction, as the loading progresses, under the action of low-intensity earthquake, the soil is further damaged compared to the situation under working condition 3, and the soil is further damaged under working condition 3. The crack started a new extension. When inputting 0.1 g Yushu wave sweep in the ZX direction under working condition 5, as the loading progresses, under low-intensity earthquakes, the soil is further damaged compared to the case under working condition 4. A series of new cracks began to appear near the diversion channel, and there was a tendency to develop to the surroundings. When inputting the 0.2 g Yushu wave sweep in the Z direction, as the loading progresses, under the action of low-intensity earthquakes, the soil is further damaged compared to the situation under the condition 5, and the slope begins to appear at the middle edge of the slope. New cracks, accompanied

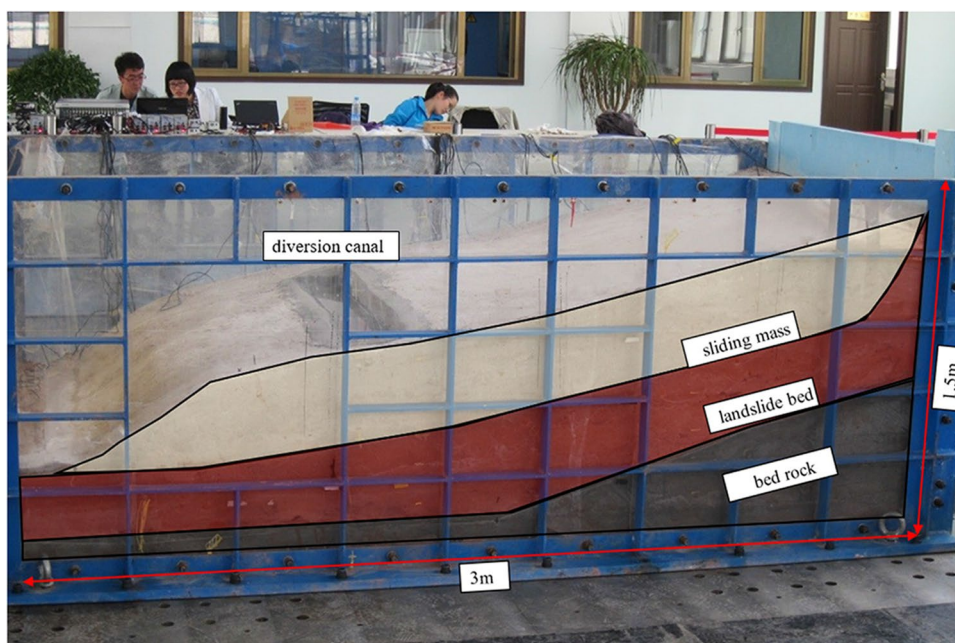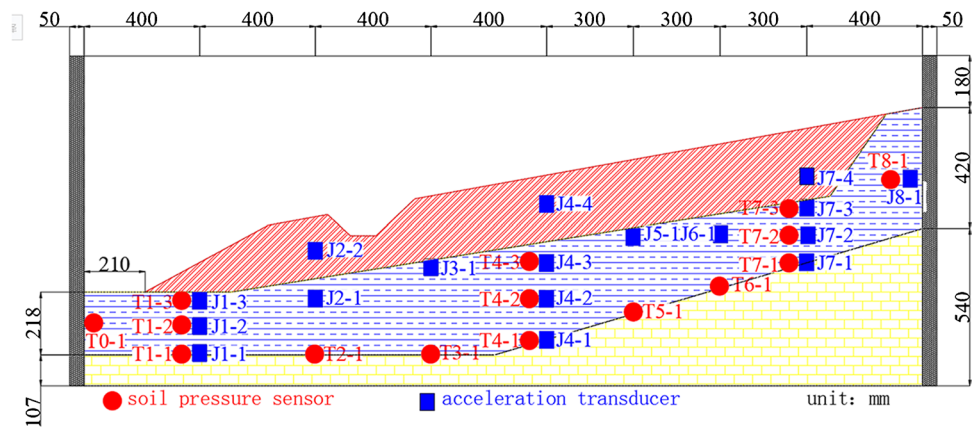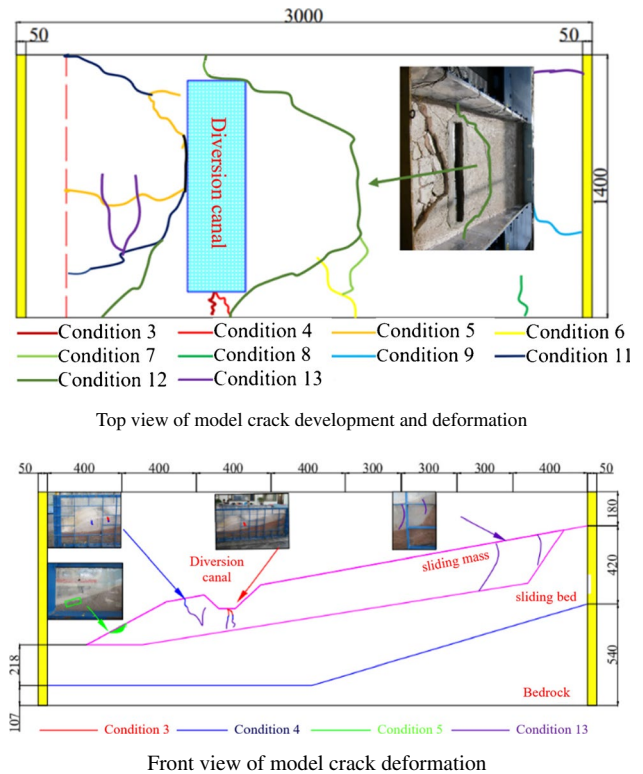**Fig. 4** Schematic diagram of Vibration model

Fig. 5 Sensor layout

Table 5 Experimental seismic wave loading conditions

Load serial number	Working condition	Table input waveform	Loading direction
1	0.1 g	Sine Wave (frequency range 3~50 Hz)	Z
2	0.1 g	Yushu Wave (UD)	Z
3	0.2 g	Sine wave (frequency range 3~50 Hz)	X
4		Yushu Wave (NS)	X
5		Yushu Wave	XZ
6		Yushu Wave (UD)	Z
7	0.2 g	Yushu Wave (NS)	X
8	0.4 g	Yushu Wave	XZ
9		Yushu Wave (UD)	Z
10	0.4 g	Yushu Wave (NS)	X
11	1.0 g	Yushu Wave	XZ
12		Yushu Wave	XZ
13	1.5 g	Yushu Wave	XZ
14	1.7 g	Yushu Wave	XZ

Top view of model crack development and deformation

Front view of model crack deformation

Fig. 6 Diagram of fracture development and deformation during the test. **a** Top view of model crack development and deformation. **b** Front view of model crack deformation

by a tendency to extend to the surroundings, and new band-shaped cracks began to appear at the bottom of the slope. When the input seismic wave is a 0.2 g Yushu wave sweep in the *X* direction, as the loading progresses, under the action of a low-intensity earthquake, the soil is further damaged compared to the situation under the condition 6, and the original is in the middle of the slope. Under the crack, a new crack began to extend. When working condition 8 is input with 0.2 g Yushu wave in ZX direction, as the loading progresses, under low-intensity earthquakes, the soil is further damaged compared with the situation under working condition 7, and the upper part of the slope begins to appear a new longitudinal crack. When working condition 9 input 0.4 g Yushu wave in the *Z* direction, as the loading progresses, under low-intensity earthquakes, the soil is further damaged compared to the situation under working condition 8, and the

slope begins to appear on the top of the slope. New longitudinal cracks. When working condition 11 enters 0.4 g Yushu wave sweep in the *ZX* direction, as the loading progresses, under low-intensity earthquakes, the soil is further damaged compared to the situation under working condition 9, and the original lower part of the slope is damaged. A series of new tension cracks began to extend near the cracks. When working condition 12 is input to 1.0 g Yushu wave sweep in *ZX* direction, as the loading progresses, under low-intensity

earthquakes, the soil is further damaged compared to the situation under working condition 11, and new slopes begin to appear at the bottom of the slope. Cracks, and began to be accompanied by small-scale fragmentation at the bottom of the slope. When working condition 13 enters 1.5 g Yushu wave sweep in the ZX direction, as the loading progresses, under low-intensity earthquakes, the soil is further damaged compared to the situation under working condition 12, and new slopes appear at the bottom of the slope. At the same time as the cracks, large-scale fragmentation began to appear.

Figure 6b shows a schematic diagram of the slope deformation of the longitudinal section of the model box during the entire test loading stage. As can be seen from the figure, for a single-slip surface landslide with diversion canal, the deformation of the slope body under the action of the earthquake first appears from the position of the diversion canal (crack generation under working condition 3), and as the test loads the lower portion of the diversion canal Cracks begin to occur at the position of the slope, and the trend of existing cracks to widen and deepen continues (the change of cracks under condition 4), and the soil at the foot of the slope becomes looser from the original compact state (action condition 5). When the input seismic wave acceleration reaches 1.5 g (condition 13), two tension cracks appear on the rear edge of the slope, and one crack penetrates from the sliding body to the position of the sliding bed. The signs of the development of the above cracks indicate that for this type of landslide, the cracks preferentially originate from the middle of the slope and develop toward the front edge of the slope. When the front slope is deformed, the trailing slope will deform and cause tension. Pull the crack.

Finite difference mechanism analysis based on point safety factor

The landslide point safety is based on the secondary development of the simulation calculation software FLAC 3D (Fast Lagrangian Analysis of Continua 2017) developed by ITASCA in the USA. FLAC 3D is a finite difference software using display Lagrangian algorithm and hybrid-discrete partitioning technology (Liu and Han 2005), which can simulate the force characteristics of the three-dimensional structure of rock and soil and other materials and analyze the plastic flow very accurately.

During the calculation of the point safety factor, the Mohr–Coulomb shear yield criterion was adopted:

$$\tau = \sigma \tan\varphi + c \tag{1}$$

In the formula: C, faiare respectively represent the cohesion and internal friction angle of the sliding zone soil.

From this, the center displacement vector of the element v can be calculated, and its components (v_x, v_y, v_z) can be characterized by the following formula

$$1-2: \begin{cases} v_x = \frac{1}{8}\sum_{i=1}^{8} u_x^i \\ v_y = \frac{1}{8}\sum_{i=1}^{8} u_y^i \\ v_z = \frac{1}{8}\sum_{i=1}^{8} u_z^i \end{cases} \tag{2}$$

In the formula:: u_x^i, u_y^i, u_z^i are respectively represent the nodal displacement components;

$$s = (n \times v) \times n \tag{3}$$

In the formula, S characterizes the actual sliding direction of the center of the unit.

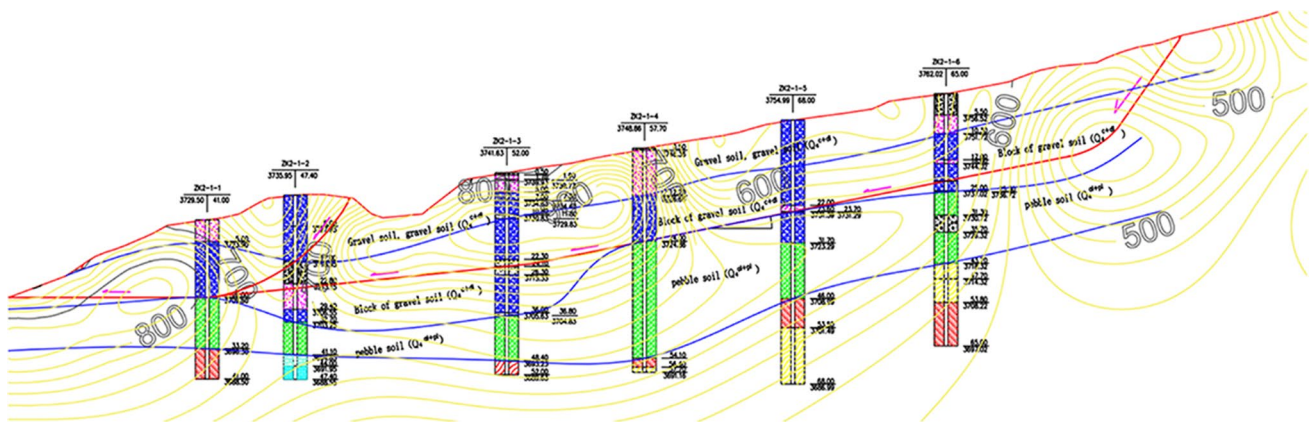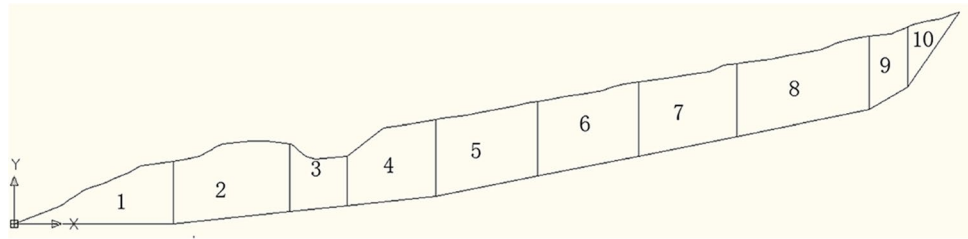The unit point safety factor F_E is defined as:

Fig. 7 Sect. 2–2

Fig. 8 Calculation model

$$F_{\mathrm{E}} = \frac{c + \sigma_{\mathrm{n}}\tan\varnothing}{\tau} \qquad (4)$$

From this, the weighted average of the slip surface area of the ball can be:

$$F_{3d} = \frac{\sum_{i=1}^{ne} F_E^i S_E^i}{\sum_{i=1}^{ne} S_E^i} \qquad (5)$$

In the formula: ne characterizes the total number of sliding belt units; F_E^i characterizes the unit point i safety factor; S_E^i characterizes the unit i sliding belt area.

Dynamic stability analysis of Airport highway 2# landslide

2# landslide belongs to accumulation layer landslide caused by earthquake. The slope is a piedmont alluvial landform, the terrain is relatively gentle, the natural slope is about 10°, and the plane is in the shape of a dustpan. The trailing edge of the landslide is distributed near the elevation of 3774 m, and the front edge is located near the top surface of the first-level terrace on the inner side of the subgrade. The left side of the landslide is connected with the 1# landslide, and the right side is developed with NW79° cracks as the boundary.

The elevation is between 3708–3735 m. The length is about 85 m, the thickness of the sliding body is about 18 m, and the volume of the sliding body is about 54.2×104 m³ (as shown in Fig. 2).

The representative cross-section is 2–2, and the 2–2 cross-section is shown in Fig. 7. The 2–2 section is selected as the calculation prototype, and the generalized calculation model is shown in Fig. 8.

Shear seismic waves propagate upward from the ground, and the acceleration is the same at the same time on the same horizontal plane. But at different heights, the seismic acceleration is different, and its magnitude depends on the distance from the point to the reference point, the seismic wave propagation speed, and the seismic wave waveform. The time difference is calculated by formula (1–1), and the acceleration of the calculation point is taken on the seismic wave waveform according to the acceleration of the reference point and the time difference from the reference point to the calculation point.

The strong shock recorded in the airport has a long-time history (80 s), but the significant impact on the stability of the landslide is between 30 and 40 s. The seismic waveform is shown in Figs. 9 and 10.

It can be seen from Fig. 11 that the overall stability coefficient is equivalent to the average stability coefficient. Some of the stability coefficients of the sliding belt are greater than 1.0, and some are greater than 1.0. Only the part with

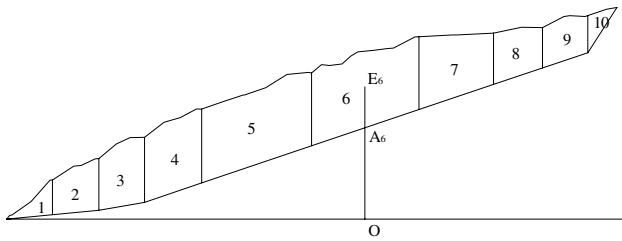**Fig. 9** EW seismic wave time-history curve (30 s ~ 40 s)
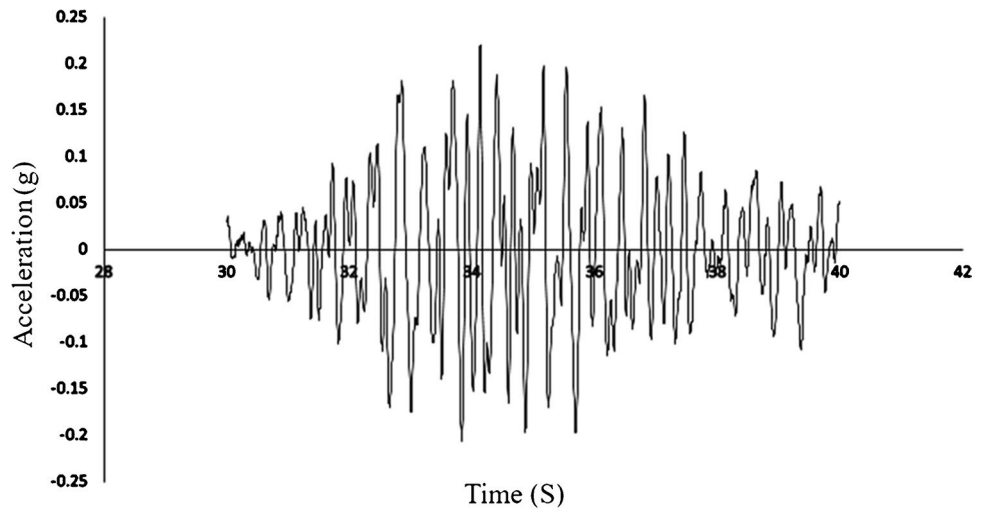
Fig. 10 Is a schematic diagram of seismic wave-loaded landslide

an instantaneous stability coefficient less than 1.0 is dominant, so the average value is less than 1.0. The instantaneous local section stability coefficient is less than 1.0, which is not enough to cause the overall instability of the landslide. In the next instant, loading in the other direction will restore the overall stability of the landslide. Therefore, the dynamic stability of the landslide body is better.

In order to compare the synchronization between the landslide stability coefficient and the seismic acceleration time history, the two variables are normalized. The processing method is:

$$y^* = \frac{y_0 - y_{\min}}{y_{\max} - y_{\min}} \tag{6}$$

In the formula: y^* is the normalized amount, y_0 is the original value, $y_{\min}$ is the sample minimum, and $y_{\max}$ is the sample maximum.

After normalization, the acceleration time history and dynamic stability time history curves are placed on a graph, as shown in Fig. 12. It can be seen that the acceleration time history and the dynamic stability time history are generally synchronized. That is, when the acceleration time in a certain direction (positive or negative) is longer (the acceleration direction conversion is slower), the synchronization

Fig. 11 Results of dynamic stability coefficient of landslide
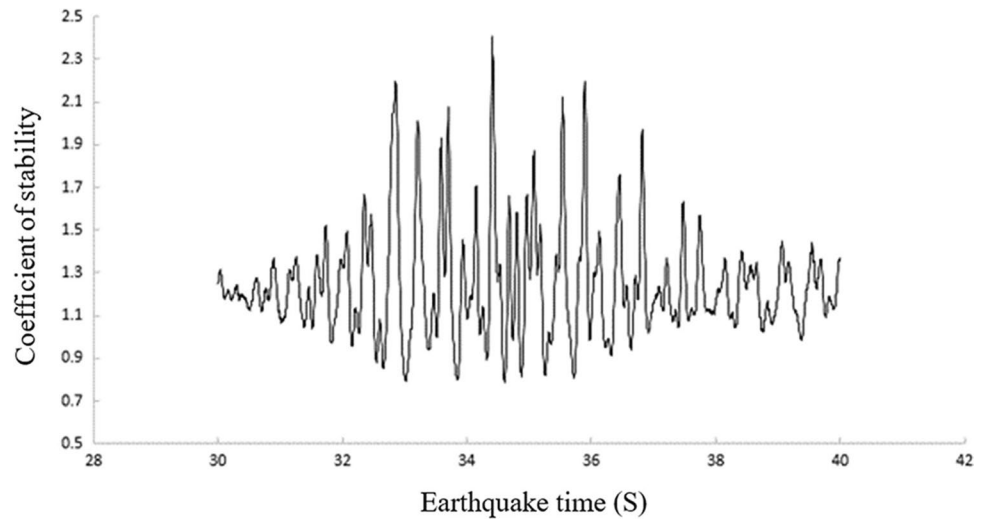
Fig. 12 Time history curve after normalization
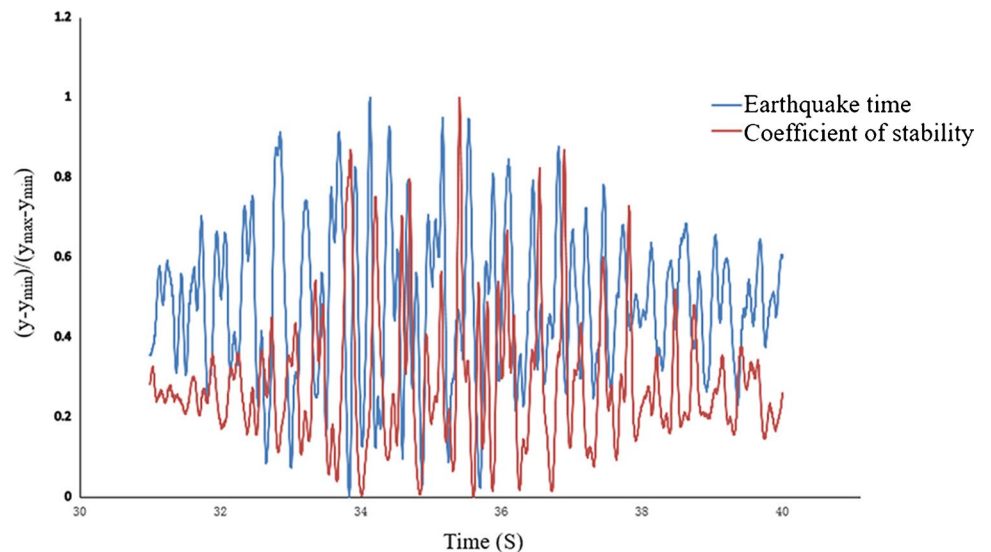
between the two is better. When the acceleration direction changes rapidly (lower acceleration and higher frequency), the synchronization between the two is poor. At the same time, it can be seen that it is not when the acceleration reaches the peak, the stability coefficient also reaches the peak (maximum or minimum), but the result of the combined action of each block (Table 6).

Analysis of dynamic instability mechanism

Taking the 2–2 section of Airport Road No. 2 landslide as a prototype, the mechanism of seismic dynamic instability is analyzed. The prototype of the landslide is shown in Fig. 13. The landslide has a length of 306.63 m and a height difference of 69.83 m. The used calculation model has a total length of 350.66 m and a thickness of 89.83 m (Figs. 14, 15, 16, 17, and 18).

The calculation parameters are shown in Table 7.

It can be seen from Fig. 19 that the landslide has a push-type sliding feature. When the front part is small and the thickness is large, the sliding mechanism of the landslide belongs to the traction type (Table 8).

Figures 20-21 show the spatial distribution of the safety factor of landslide points. From this, it can be seen that the overall safety factor of the landslide is gradually decreasing due to dynamic effects.

The point safety factor changes periodically with the dynamic process. In the same seismic wave action period, the safety factor of different unit points in the sliding zone does not reach the maximum at the same time, but there is a certain hysteresis. At the same time, the spatial distribution of the safety factors of different unit points reflects the spatial stability of the sliding zone, that is, the stability of different parts, which is conducive to the analysis of the instability mechanism of the landslide.

Table 6 Calculation model geometric parameters

| Slider number	1	2	3	4	5	6	7	8	9	10
Area (m^2)	563.814	835.351	314.003	630.111	782.821	757.144	727.023	966.342	254.910	157.534
Length of bottom sliding surface (m)	50.850	37.303	18.554	28.472	33.232	32.803	32.196	43.097	14.209	29.048
Sliding surface inclination (°)	0.000	5.920	5.920	5.920	11.310	11.310	11.310	11.310	30.630	55.350
Height of midpoint of sliding surface (m)	0.000	1.923	4.802	7.225	11.951	18.424	24.796	32.178	40.022	55.590
Center height of block (m)	7.396	13.273	13.359	18.587	23.952	30.194	36.302	43.644	50.361	57.947
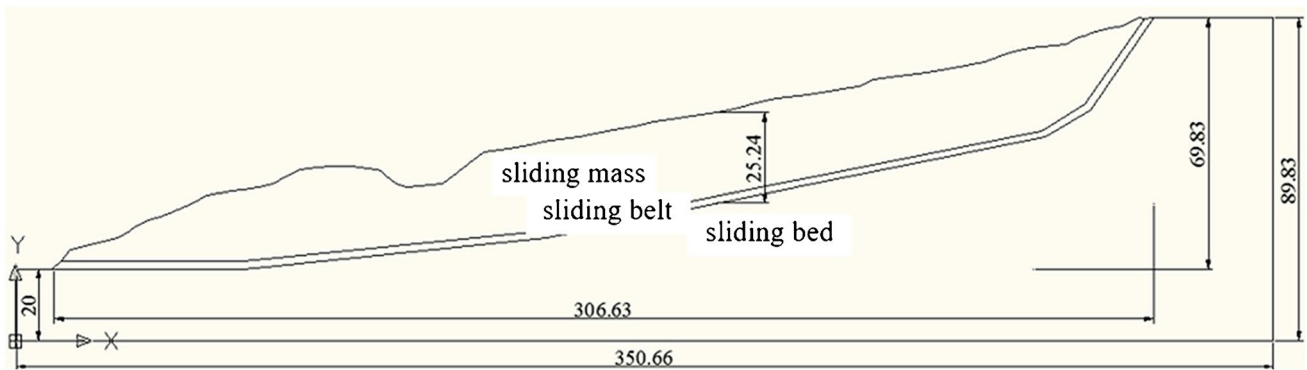
Fig. 13 Calculation prototype

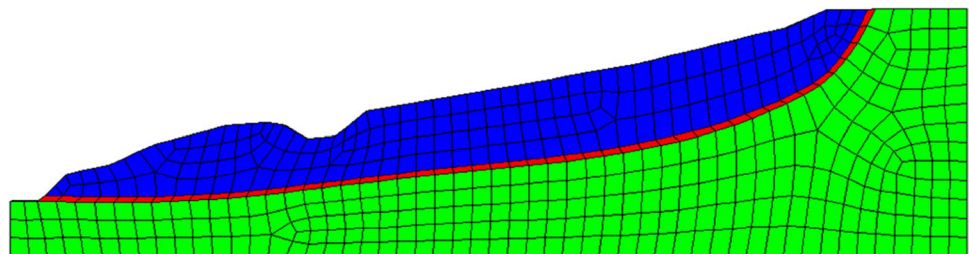**Fig. 14** Numerical simulation grid

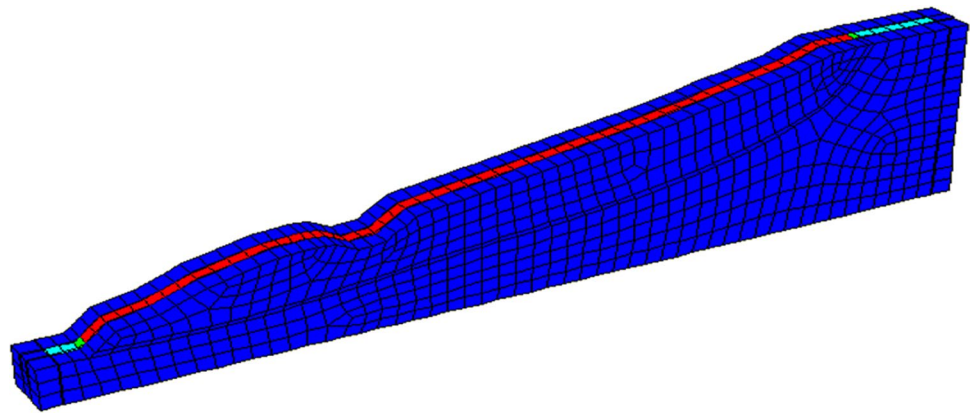**Fig. 15** Free field boundary for dynamic calculation

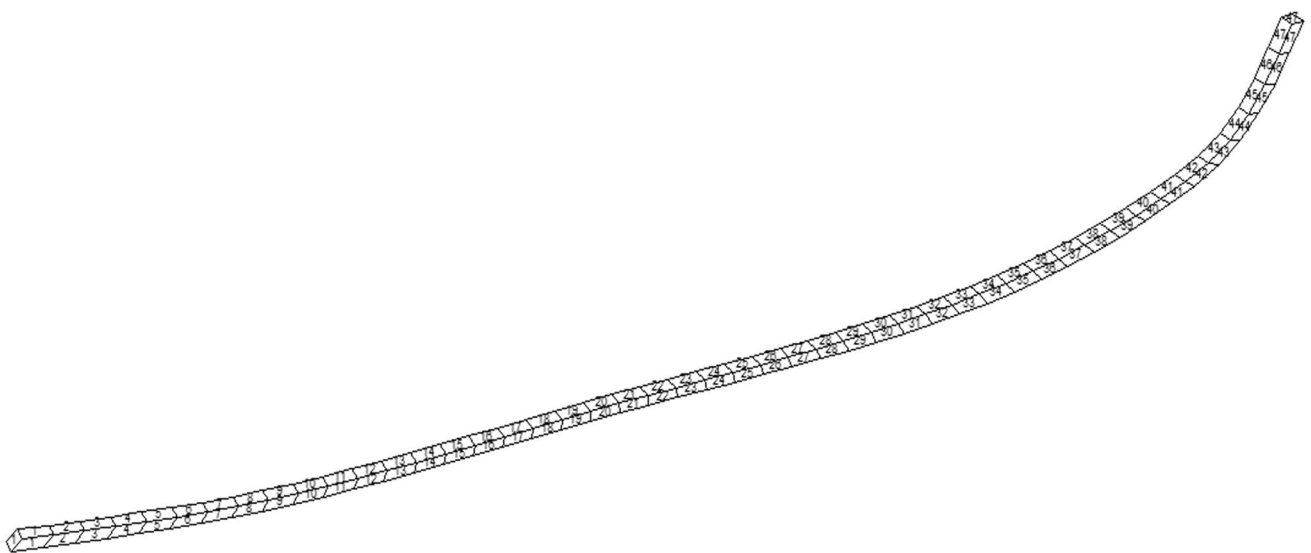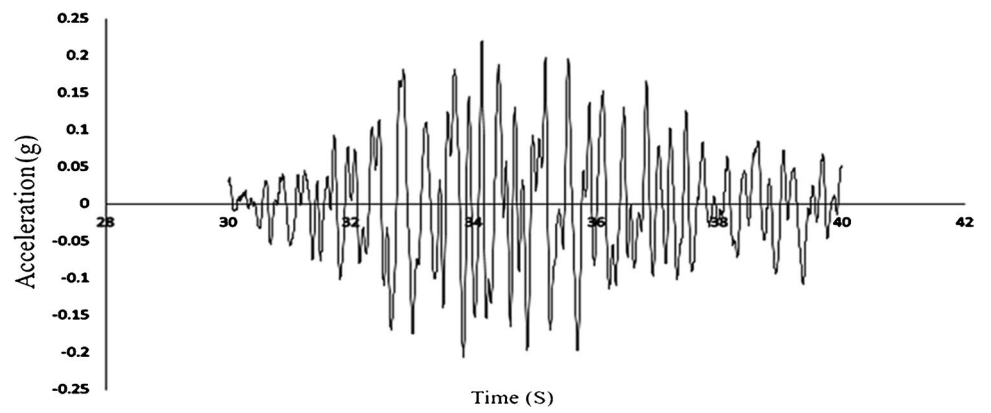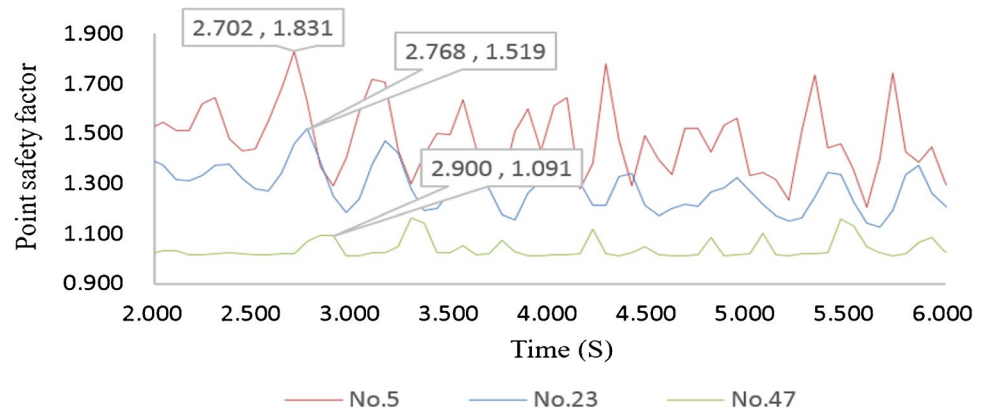**Fig. 16** EW-trending seismic wave time-history Curve (30 s ~ 40 s)

Fig. 17 Slide strip unit number

Fig. 18 Peak lag phenomenon of safety factor

The blocking effect of the sliding belt on the acceleration amplification factor

From the analysis of the sliding mechanism, under the action of an earthquake, the acceleration amplification coefficient has a significant hysteresis effect due to the elevation difference of each point in the slope. In order to further analyze the distribution law of the acceleration amplification coefficient, on this basis, the acceleration amplification is proposed. Coefficients and methods for landslide stability analysis during seismic wave propagation.

Model establishment

In the analysis of landslide stability, the quasi-static method is widely used because of its simple formula, convenient use, and familiarity with engineering circles. In the pseudo-static method, the seismic load is simplified as a static force in the horizontal direction.

$$F = a \cdot G$$

Therefore, the value of the seismic coefficient α is very important.

Firstly, the distribution law of acceleration magnification coefficient in landslide body is discussed here. The acceleration amplification factor is defined as the ratio of the peak value of the response acceleration time history curve of each

point in the slope to the peak value of the input acceleration time history at the bottom of the model. Has the meaning of relatively increasing proportions.

Taking the 2–2 section of airport highway No. 2 landslide as a prototype, the seismic dynamic response analysis was carried out, and the distribution law of landslide acceleration amplification coefficient was discussed. The prototype of the landslide is shown in Fig. 2.

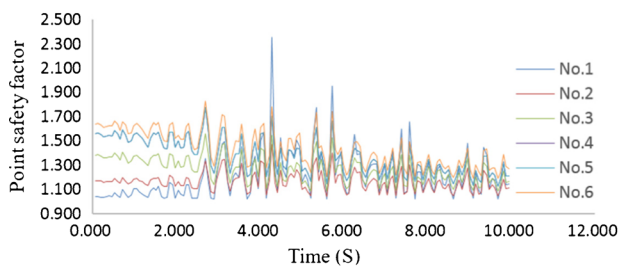The calculation parameters are shown in Table 9.

Result analysis

The state of the elastic sliding belt

In order to simulate the different mechanical states of the sliding zone soil, first adjust the shear strength parameters of the sliding zone soil to make its cohesion and internal friction angle °. The calculated result is shown in Fig. 22.

It can be seen from the calculation results that due to the high shear strength parameters of the sliding zone soil, under the static state of its own weight, the sliding zone soil is not completely in the state of shaping and yielding, only the back section of the sliding zone is in the state of shaping and yielding. The distribution characteristics of this plastic zone remain under dynamic action, as shown in Fig. 22b. Judging from the distribution of the plastic zone, the sliding zone effect is not obvious, and it can be considered that the entire calculation domain of the slope body is in an elastic state.
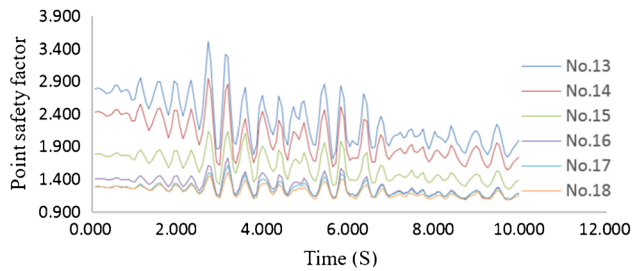
Table 7 Calculation parameters

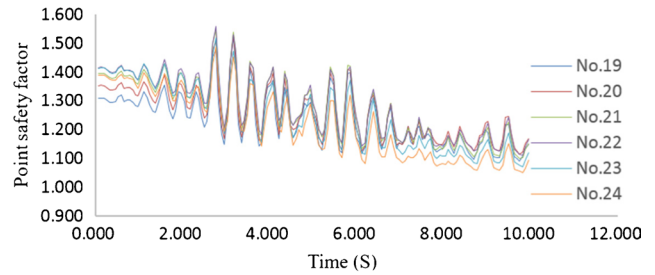| Rock body category	Elastic modulus/MPa	Poisson ratio	Cohesion/kPa	angle of internal friction/(°)	Gravity/ (kN/ m³)
Sliding mass	80	0.3	120	30	20
sliding belt	30	0.35	14 (12)	12 (10)	19
Sliding bed	1000	0.25	200	38	21

Time-history curve of point safety factor (No.1~No.6)
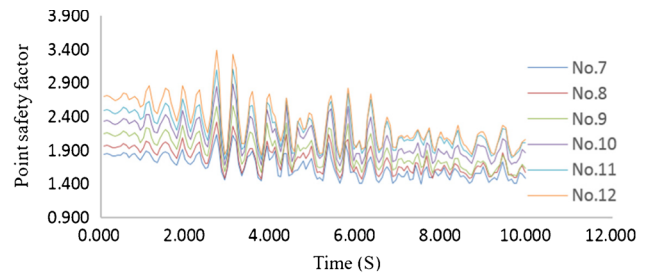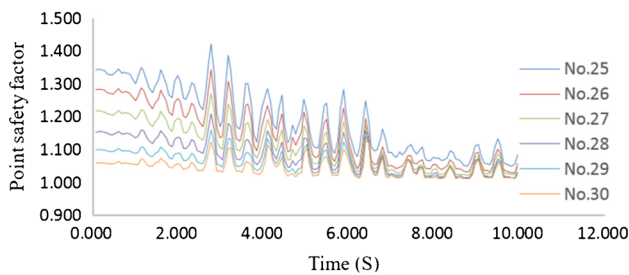

Time-history curve of point safety factor (No.7~No.12)
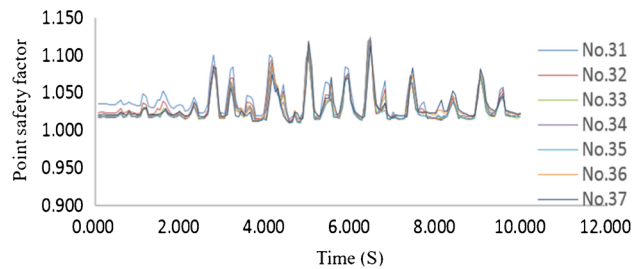

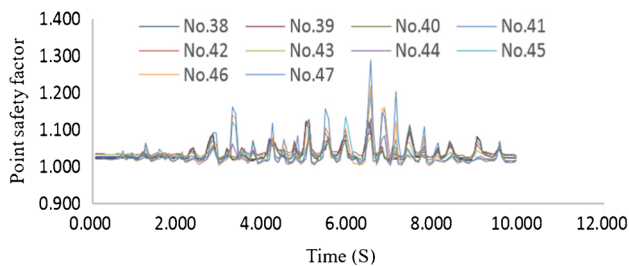Time-history curve of point safety factor (No.13~No.18)

Time-history curve of point safety factor (No.19~No.24)

Time-history curve of point safety factor (No.25~No.30)

Time-history curve of point safety factor (No.31~No.37)

Time-history curve of point safety factor (No.38~No.45)

Fig. 19 Time-history curve of safety factor. **a** Time-history curve of point safety factor (No.1~No.6). **b** Time-history curve of point safety factor (No.7~No.12). **c** Time-history curve of point safety factor (No.13~No.18). **d** Time-history curve of point safety factor (No.19~No.24). **e** Time-history curve of point safety factor (No.25~No.30). **f** Time-history curve of point safety factor (No.31~No.37). **g** Time-history curve of point safety factor (No.38~No.45)

At this time, the distribution law of acceleration amplification coefficient in the slope is shown in Fig. 22c. On the whole, the magnification factor of the lower part of the slope is small, and the magnification factor of the upper part of the slope is larger. The magnification factor shows a development trend that gradually increases with the height, and is basically continuous at the sliding surface.

Table 8 Safety coefficient of reverse point of some units at earthquake time (0.130~0.545)

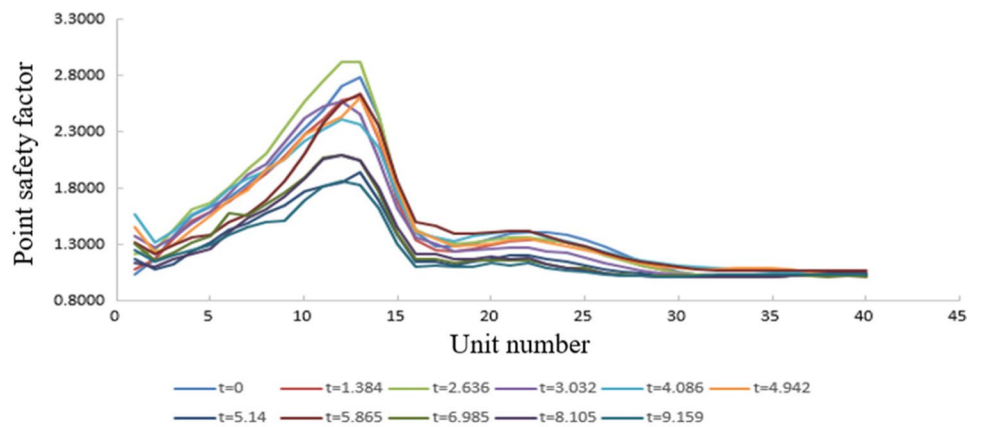| Time	No.23	No.24	No.25	No.26	No.27	No.28	No.29	No.30	No.31	No.32	No.33
0.130	1.31	1.31	1.32	1.34	−1.36	−1.38	−1.40	−1.40	−1.40	−1.39	−1.38
0.156	1.30	1.31	1.32	−1.34	−1.36	−1.38	−1.40	−1.40	−1.40	−1.39	−1.38
0.182	1.31	1.31	1.32	−1.34	−1.36	−1.38	−1.40	−1.40	−1.40	−1.39	−1.37
0.208	1.31	1.31	−1.33	−1.34	−1.36	−1.38	−1.40	−1.40	−1.40	−1.39	−1.38
0.234	1.31	1.32	−1.33	−1.35	−1.37	−1.39	−1.40	−1.41	−1.40	−1.39	−1.38
0.260	1.32	−1.32	−1.33	−1.35	−1.37	−1.39	−1.41	−1.41	−1.41	−1.40	−1.38
0.286	1.32	−1.32	−1.34	−1.35	−1.38	−1.40	−1.41	−1.42	−1.41	−1.40	−1.39
0.311	1.32	−1.32	−1.34	−1.36	−1.38	−1.40	−1.41	−1.42	−1.42	−1.41	−1.39
0.337	1.31	−1.32	−1.33	−1.35	−1.37	−1.39	−1.41	−1.42	−1.41	−1.40	−1.39
0.363	1.31	−1.32	−1.33	−1.35	−1.37	−1.39	−1.41	−1.41	−1.41	−1.40	−1.39
0.389	1.31	−1.31	−1.33	−1.34	−1.37	−1.39	−1.40	−1.41	−1.40	−1.39	−1.38
0.415	1.31	1.31	−1.32	−1.34	−1.36	−1.38	−1.40	−1.40	−1.40	−1.39	−1.38

Fully shaped sliding belt state

In order to further analyze the distribution law of acceleration amplification coefficient when the sliding zone soil is in a fully shaped state, the shear strength parameters of the sliding zone are reduced to cohesion $c = 8$kPa, the internal friction angle $°\varphi = 8°$, and the calculation results are shown in Fig. 23.

It can be seen from the calculation results that due to the low shear strength parameters of the sliding zone

Fig. 20 Distribution of safety factors at slip points. **a** Distribution of safety factor of slip band point (-). **b** Distribution of safety factor of slip band point ( )

Distribution of safety factor of slip band point （一）
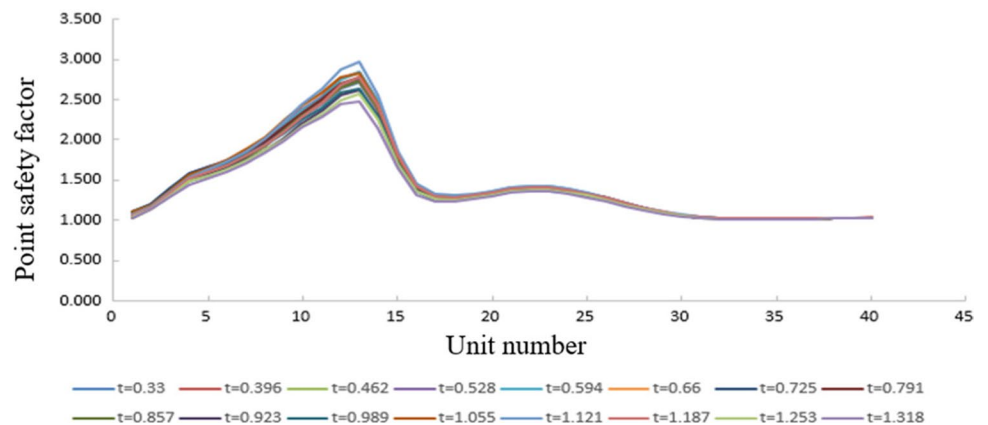
Distribution of safety factor of slip band point （二）

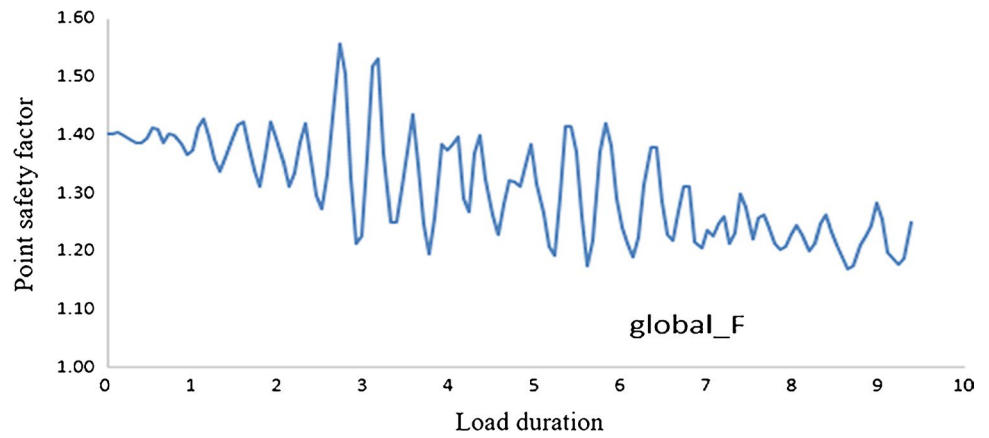**Fig. 21** Overall safety factor time history

Table 9 Calculation parameters

Rock body category	Elastic modulus/MPa	Poisson ratio	Cohesion/kPa	angle of internal friction/(°)	Gravity/(kN/m³)
Sliding mass	80	0.3	120	30	20
sliding belt	30	0.35	14 (12)	12 (10)	19
Sliding bed	1000	0.25	200	38	21

Fig. 22 Acceleration amplification factor of elastic slip band. **a** Static state. **b** Dynamic status. **c** Acceleration amplification factor distribution
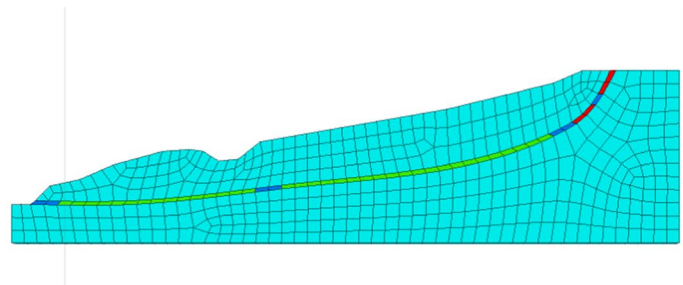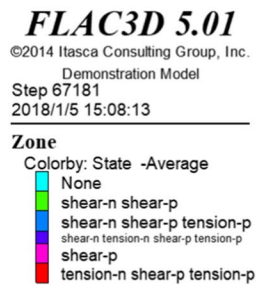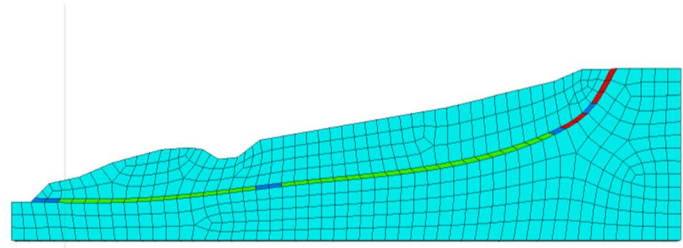

Static state

Dynamic status

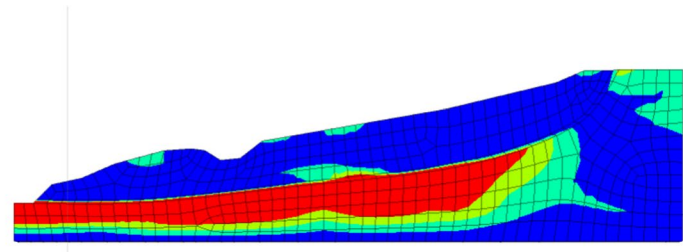Acceleration amplification factor distribution
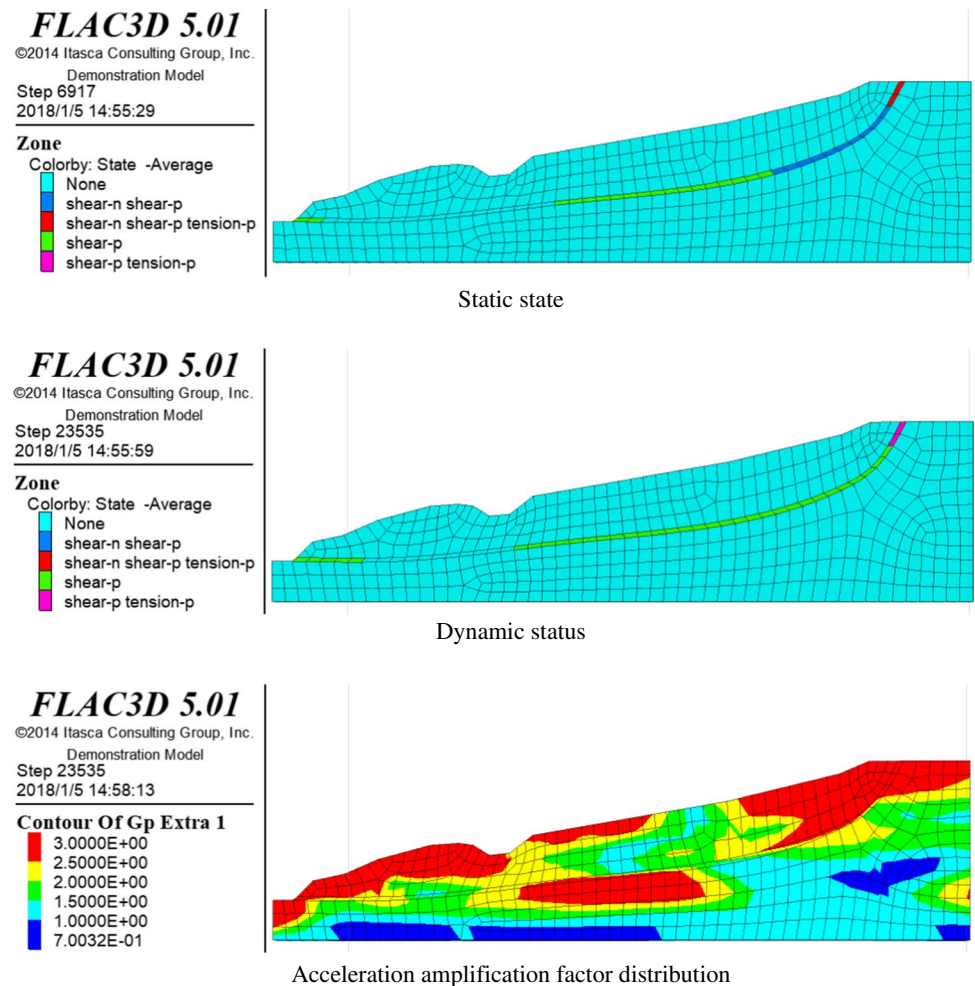
Fig. 23 Acceleration amplification factor of fully molded slide strip. **a** Static state. **b** Dynamic status. **c** Acceleration amplification factor distribution

Static state

Dynamic status

Acceleration amplification factor distribution

soil, under the static state of its own weight, the sliding zone soil is completely in the plastic yielding state, and is in the current plastic yielding state. The distribution characteristics of this plastic zone remain under dynamic action, as shown in Fig. 23b. From the distribution of the plastic zone, the effect of the sliding zone is obvious, and its yield state is greatly different from that of the slope. It can be considered that the entire sliding zone soil is in a plastic state.

At this time, the distribution law of acceleration amplification coefficient in the slope is shown in Fig. 23c. It can be seen that the magnification factor in the sliding bed is obviously different from that in the sliding body. The rock-soil mass of the sliding bed is in an elastic state as a whole, and the magnification factor presents a trend of smaller lower part and larger upper part. For the sliding body, the magnification factor is almost the same as the bottom of the model, that is, there is no magnification effect.

It can be seen that the sliding zone soil has an obvious blocking effect on the acceleration amplification effect of the landslide body. When the sliding zone soil is in an elastic state, the sliding zone soil has little effect on the dynamic acceleration amplification effect of the slope, and the amplification factor is mainly affected by the terrain, showing the effect of amplification with the increase in height(Bing 2012; Sun et al. 2015; Ma and Zhou 2013; Lu 2015; Li et al. 2014; Chen and Xia 2016; Qin 2008). When the sliding zone soil is in a plastic yielding state, the ground motion energy is absorbed by the sliding zone soil during the upward propagation process and converted into plastic strain. It is difficult to continue to transmit the load upwards, so the acceleration peak does not increase.

Under the current parameter state, the acceleration amplification factor distribution of the slope body is shown in Fig. 24. In the process of stress adjustment, the sliding belt is in a plastic yielding state, especially when the second half of the sliding belt yields obviously, the acceleration amplification factor is amplified to a certain extent in the front part, but there is no amplification effect in the back part of the landslide body.

Fig. 24 Amplification factor of acceleration of the current slope. **a** Dynamic status. **b** Acceleration amplification factor distribution
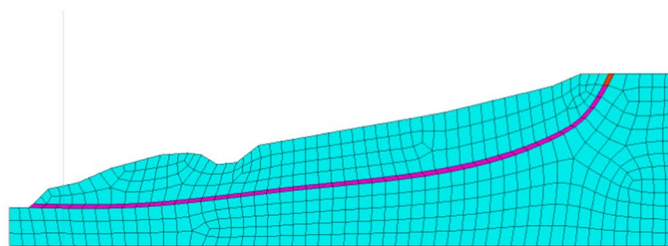
Dynamic status

Acceleration amplification factor distribution

Conclusion

Through the shaking table test and numerical calculation analysis of single-sliding surface accumulation landslide under earthquake action, it can be known that:

1. Through the analysis of the shaking table test phenomenon, it can be seen that cracks appeared at both ends of the slope first during the shaking process. With the progress of the test, cracks appeared in the middle of the slope, and the soil at the foot of the slope was largely broken, and the entire slope surface was sliding downwards trend.

2. From the calculation of the safety factor of the landslide point of the 2# and 3# single-sliding surface accumulation layer on the airport road, it can be seen that the sliding process of the 2# landslide exhibits the characteristics of pushing slip. Affected by the dynamic process, the safety factor of the landslide body has obvious fluctuations, and the overall safety factor continues to decrease.

3. Sliding zone soil has an obvious blocking effect on the acceleration amplification effect of the landslide body.

When the sliding zone soil is in an elastic state, the sliding zone soil has little effect on the dynamic acceleration amplification effect of the slope. The amplification factor is mainly affected by the terrain, showing the effect of amplification as the height increases. When the sliding zone soil is in a plastic yielding state, the ground motion energy is absorbed by the sliding zone soil during the upward propagation process and converted into plastic strain. It is difficult to continue to transmit the load upwards, so the peak acceleration does not increase.

Declarations

Conflict of interest The authors declare no conflict of interest.

References

Arango I, Seed HB (1974) Seismic stability and deformation of clay slopes[J]. J Geotech Eng Div (ASCE) 100(2):139–156

Bing G (2012) Research on the development characteristics and prevention measures of geological hazards along the Yingwen Highway after the "5.12" Wenchuan earthquake [D]. Chengdu University of Technology

Cai M, He M, Liu D (2002) Rock Mechanics and Engineering. Science Press, Beijing

Celebi M (1987) Topographical and geological amplifications determined from strong-motion and aftershock records of the 3 March 1985 Chile earthquake[J]. Bull Seismol Soc Am

Chen Z (2003) Stability analysis of soil slope—principle·method·procedure [M]. China Water Power Press, Beijing

Chen X, Shen J, Wei P, Yang J (2010) Large-scale shaking table test study on the seismic stability of Xiashu soil slopes (II)-test results and analysis[J]. J Disaster Prev Mitig Eng 30(06):587–594

Clough RW, Pirtz D (1956) Earthquake resistance of rock fill dams[J]. J Soil Mech Found Div 82(2):1–26

Chen C, Xia Y (2016) Real-time dynamic Newmark slider displacement method for slopes based on limit analysis[J]. Chin J Rock Mech Eng 035(012):2507–2515

Coates DF (1970) Rock Mechanics principles (Revised). Quebec, Ottawa

Del Gaudio V, Wasowski J (2007) Directivity of slope dynamic response to seismic shaking [J]. Geophys Res Lett 34:L12301

Dong J, Yang G, Wu F, Qi S (2011) Large-scale shaking table test study on dynamic response and failure modes of bedding rock slopes under earthquake[J]. Rock Soil Mech 32(10):2977–2983

Feng W, Huang R, Xu Q, Xiao R (2009) Research on the formation mechanism and deformation and failure modes of shattered slopes[J]. Hydrogeol Eng Geol 36(06):42–48

Gong X (2001) Geotechnical computer analysis. China Construction Engineering Press, Beijing

Hong YS, Chen RH, Wu CS, Chen JR (2005) Shaking table tests and stability analysis of steep nailed slopes[J]. Can Geotech J 42(5):1264–1279

Hu G (1995) Landslide dynamics[M]. Geological Publishing House, Beijing

Huang X, Li Z, Ding Y (2008) Analysis and research on seismic design of houses in villages and towns in my country [C]// National Civil Engineering Postgraduate Academic Forum

Hutchinson JN (1989) General report: morphological and geotechnical parameters of landslides in relation to geology and hydrogeology Proc 5th International Symposium on Landslides, Lausanne, 10–15 July 1988V1, P3–35. Publ Rotterdam: A A Balkema, 1988[J]. Int J Rock Mech Mining ences Geomech Abstr 26(2):88–88.

Itasca Consulting Group Inc. FLAC-3D (Fast Lagrangian analysis of continua in 3 dimensions) Version 6.00 Users Manual (Volume) [R]. USA Itasca Consulting Group Inc 2017l

Keefer DK (1984) Landslides caused by earthquakes[J]. Geol Soc Am Bull 95:406–421

Li S (1999) Research on Active Fault Segmentation[J]. J Peking Univ (Natural Science Edition) 06:3–5

Li Y (1997) Application of reliability analysis in slope stability calculation. J Wuhan Inst Chem Technol 12 19(3):31–35

Li M, Xin H, Sun L (2014) Newmark slider analysis method to evaluate the seismic stability of soil slopes[J]. Industrial Construction (S1):722–726

Lin ML, Wang KL (2006) Seismic slope behavior in a large-scale shaking table model test[J]. Eng Geol 86(2–3):118–133

Ling HI, Mohri Y, Leshchinsky D et al (2005) Large-scale shaking table tests on modular-block reinforced soil retaining walls[J]. J Geotech Geoenviron Eng 131(4):465–476

Liu H, Bo J, Liu D (2007) Research progress in seismic stability evaluation of rock-soil slopes[J]. J Inst Disaster Prev Sci Technol (03): 20–27 (Li.1999; Liu)

Liu B, Han Y (2005) FLAC principle examples and application guide [M]. People's Communications Press

Lu Y (2015) Research on the safety evaluation method of rock slope under seismic load[D]

Luo G, Wang P, Wu H etc (1981) Analysis of stability and failure mechanism of Fuxikou loosely deformed slope[J]. Hunan Water Resour (1): 12–16.

Liu H, Zhu X (1999) Observation and research progress of terrain magnification effect in earthquake[J]. World Earthq Eng (03): 3–5

Ma L, Zhou X (2013) Analysis of cracks in masonry structures under earthquake damage[J]. Architectural Engineering Technology and Design 000(001):186–186

Ma et al (2019) Ground motions induced by mining seismic events with different focal mechanisms. Int Rock Mech Min Sci 116:99–110

Ma et al (2018) Qualitative method and case study for ground vibration of tunnels induced by fault-slip in underground mine. Rock Mech Rock Eng. https://doi.org/10.1007/s00603-018-1631-x

Mao Y, Hu G, Mao X, Shi Y (2001) Study on the mechanism and discrete element simulation of seismic landslide start-up turbulence[J]. J Eng Geol (01): 74–80.

Ma Z, Ma Z (2007) Natural disasters and disaster mitigation countermeasures in China (Part 3)—Earthquake disasters and countermeasures in my country[J]. J Inst Disaster Prev Sci Technol 9(001):1–5

Qi S, Wu F, Liu C, Ding Y (2004) Engineering geological analysis of seismic slope stability[J]. Chin J Rock Mech Eng (16): 2792–2797

Qin S (2008) Research on static nonlinear analysis method of bridge seismic performance evaluation [D]. Dalian University of Technology

Qu H, Zhang J, Wang F (2013) Shaking table test study on seismic response of prestressed anchor-cable pile-slab wall[J]. Chin J Geotech Eng 35(2):313–320

Qu H, Zhang J (2012) Shaking table test study on the influence of foundation conditions on the seismic earth pressure of retaining walls[J]. Chin J Geotech Eng 34(7):1227–1233

Seed HB, Clough RW (1963) Earthquake resistance of sloping core dams[J]. J Soil Mech Found Div 89(1):209–242

Shi G (1977) Stereoscopic projection method for rock stability analysis [J]. Sci China 3:260–271

Shimizu Y, Aydan ö, Ichikaw Y (1986) A model study on dynamic failure modes of discontinuous rock slopes. Proceedings of the International Symposium on Engineering in Complex Rock Formations[C]. Int Soc Rock Mech. 7

Sokolovsky (1956) The statics of loose media. Seismological Press, Beijing

Sloan SW (1989a) Lower bound limit analysis using finite elements and linear programming. Int J Numer Anal Meth Geomech 12:61–67

Sloan SW (1989b) Upper bound limit analysis using finite elements and linear programming. Int J Numer Anal Meth Geomech 13:263–282

Sun Y, Gu X (1980) The application of stereographic projection in rock engineering geomechanics. Science Press

Sun Y, Mou H, Yao B (1988) Stability analysis of slope rock mass. Beijing: Science Press

Sun J (2007) Simulating seismic shaking table test of complex tall steel structure[D]. Master's degree thesis of University of Science and Technology Beijing

Sui X (2009) Research on the seismic isolation performance of rubber particles-sand mixture[D]. Hunan University

Sun Z, Kong L, Guo A et al (2015) Slope deformation and instability mechanism of accumulation body slope under earthquake[J]. Rock Soil Mech 36(No. 253(12)):3465–3472

Wartman J, Seed RB, Bray JD (2005) Shaking table modeling of seismically induced deformations in slopes[J]. J Geotech Geoenviron Eng 131(5):610–622

Wang KL, Lin ML (2011) Initiation and displacement of landslide induced by earthquake—a study of shaking table model slope test[J]. Eng Geol 122(1–2):106–114

Xiong W (2009) Research on a new distributed seismic isolation system based on SSI and nonlinear soil response[D]. Hunan University

Xu G, Yao L, Gao Z, Li C (2008) Large-scale shaking table model test study on slope dynamic characteristics and dynamic response[J]. Chin J Rock Mech Eng 27(3):624–632

Wang F (2012) Equivalent modeling method and seismic response analysis of shield tunnel[D]. Shanghai Jiaotong University

Xia Y, Zhu R, Li X (1995) Summary and prospect of research on slope stability. Metal mines (12): 9–12

Yang G, Wu F, Dong J, Qi S (2012a) Research on dynamic response characteristics and deformation failure mechanism of rock slope under earthquake[J]. Chin J Rock Mech Eng 31(4):696–702

Yang G, Ye H, Wu F, Qi S, Dong J (2012b) Shaking table model test on dynamic response characteristics and failure mechanism of rock slope with anti-dipping layered structure[J]. Chin J Rock Mech Eng 31(11):2214–2221

Yang C, Zhang J, Zhou D (2013a) Research on time-frequency analysis method of seismic stability of rock slope under SV wave[J]. Chin J Rock Mech Eng 32(3):483–491

Yang C, Gao H, Zhang J (2013b) Similarities and differences in seismic dynamic response of high and steep rock slopes[J]. J Sichuan Univ (Eng Sci Ed) 45(3):18–26

Yang C, Zhang J, Zhang M, Yao S (2013c) Study on the mechanism of earthquake landslides on double-sided high-steep rock slopes[J]. Rock and Soil Mech 34(11):3261–3268

Ye H, Zheng Y, Du X, Li A (2012a) Shaking table model test and numerical analysis of slope dynamic failure characteristics[J]. Chin Civil Eng J 45(9):128–135

Ye H, Zheng Y, Lu X, Li A (2011) Shaking table test study on the ground motion characteristics of slope anchors[J]. Chin Civil Eng J 44(supplement):152–158

Ye H, Zheng Y, Li A, Du X (2012b) Shaking table test study on slope anti-slide piles under earthquake[J]. Chin J Geotech Eng 34(2):251–257

Ye H, Zheng Y, Li A, Du X (2012c) Shaking table test study of slope prestressed anchor cable under earthquake[J]. Chin J Rock Mech Eng 31(1):2847–2854

Zhang P, Wu D (1997) Experimental study on slope sliding under dynamic load[J]. J Chongqing Jianzhu Univ 02:85–91

Zhang Z, Wang S, Wang L (1993) Principles of engineering geology analysis [M]. Geological Publishing House, Beijing

Zhang Y, Xu L, Chen Y (2010) The focal process of the Yushu earthquake in Qinghai in 2010[J]. Sci China Earth Sci 40(07):819–821

Zheng Y, Zhao S (2004) Application of finite element strength reduction method in soil slope and rock slope[J]. Chin J Rock Mech Eng (19):3381–3388